# A New Web-type Concept of Floating Photovoltaic Farms in Open Sea Environment

Zhi-Ming Yuan, Shuang-Rui Yu, Atilla Incecik

Department of Naval Architecture, Ocean and Marine Engineering, University of Strathclyde, Glasgow, G4 0LZ, UK

## Abstract

The development of floating photovoltaic (FPV) technologies has grown rapidly. Although there are concepts proposed to be operated in the ocean, the survivability of FPV system in harsh marine environment remains a key challenge, particularly under large wave impact loads. To address this issue, a step change in design is urgently desired. Natural structures are renowned for exquisite designs. Web-spinning spiders are sedentary predators that depend crucially on the performance of their silken webs which over time have evolved to cover a large area and withstand extreme weather conditions and impact loads with minimum material. Those remarkable features of spider webs are exactly what we would like to adapt in order to address the challenges raised for the next generation of FPV system. In this study, a nature-based design concept is proposed, in which a bio-inspired web-type floating structure is designed to support FPV modules. This fully flexible and modular design can mitigate the impact loads by deforming in waves. The technical feasibility of such a new design concept is evaluated by using the Morison model. Different configurations of FPV webs are investigated to analyse the effects of environmental loads and design parameters. The motion responses and variations in mooring loads are compared under various wave conditions. The results indicate that for the proposed web-type structures, the rope connection could maintain the overall motion at a low level, while the peak mooring tensions can also be optimised. By tuning the gap between modules, the pretension on the connecting mooring lines can be optimised. Additionally, the dynamic performance of a large FPV system is evaluated. The feasibility of the proposed concept is confirmed through these analyses.

## Keywords:

Floating photovoltaic; Conceptual design; Flexible connection; Dynamic response; Floating multi-body system

## 1 Introduction

The floating photovoltaic (FPV) energy market has grown rapidly since 2016, reaching an installed capacity of 3 GW by 2020. There are more than 60 countries joining the FPV campaign and the total capacity is expected to increase to 10-30 GW by 2030 [1]. However, the technologies developed from these FPV projects are mainly practical in calm, inland water bodies, limiting their applicability in dynamic offshore environments [2]. While several concepts have been proposed for ocean-based FPV, the technologies underdeveloped for reliable operation in harsh sea conditions. A significant advancement in design is urgently required to enable FPV systems to operate reliably and efficiently in offshore environments over extended periods.

In recent years, modular solutions have gained traction within the ocean renewable energy field. Modularised arrays offer the advantage of easy installation and disassembly, making them highly adaptable for scalability [3,4]. They have the potential to be expanded, with its size ranging from tens to thousands of meters, depending on specific deployment requirements. Such system could also help minimise hydroelastic structural issues compared to integrated large structures [5]. Modularised arrays can be applied to various types of engineering structures, such as wave energy converter (WEC) arrays [6–9], aquaculture platforms [10], and floating solar panels [11,12], to mitigation the motion and load induced by waves, current and wind. These structures often require large number of connections to accommodate the demands of both power generation and space utilisation of aquaculture [10,13].

The connection methods between floating modules include flexible connection methods such as hinge or ball joint [13,14], elastic connection [15], and rigid connection [16] methods. A common connection method is the hinged connection, which only allows for rotation between modules while providing structural stability. Researchers have thoroughly investigated the motion responses and load distribution of hinged floating bodies under various wave conditions. Noad and Porter [17] compared device proportions, hinge position and number of pontoons of an articulated raft WEC. They found that placing longer pontoons to the aft is beneficial to the power performance of system. Pelamis [8,9] was designed to absorb wave energy from the rotational motion between 4 to 5 hinged tube segments. Its dynamics show good energy capture efficiency and extreme wave condition resistance. Zhang et al. [18] focused on investigating the motion behaviour of large arrays formed by multiple floaters hinged together. Their research found that the heave motion of the array subjected to hinge constraints was significantly suppressed, but a strong pitch motion occurred in a larger wavelength range.

Using hinged connector for rigid modules is also one of main strategies for flexible FPV solutions [19]. SolarDuck [11] developed a triangular FPV module concept, flexibly connected and moving with the waves to be more compliant with wave loads. Wei et al. [20] assessed the motion characteristics of modularised floaters with hinge connection in waves. The ratio of structure length to wavelength was found to be a crucial parameter influencing the heave and pitch motions of the modular solar farm. Ji et al. [21] designed three types of connectors to integrate six floating modules into a FPV system. Numerical simulations indicate that the design featuring ball joints aligned with the wave propagation direction offers best performance. Another flexible FPV solutions is using membranes to support PV modules, such as Ocean Sun [22], DNV SUNdy [23], and MIRARCO project [24]. It should be noted that the feasibility of these thin-film concepts is facing significant challenges due to failures observed in prototype tests and pilot projects.

Although the use of hinged or joint connectors for stiff modules to form large arrays has been a popular area of research, these systems are generally classified as semi-flexible connections. These connections are particularly vulnerable to damage or failure when subjected to continuous wave impact and the associated dynamic loading. Some flexible connections, particularly rope connections, have gained great interest due to their ability to absorb energy and redistribute loads more evenly across the structure. The flexible connection has lower torque and shear force compared to mechanical joints. Jiang et al. [15] conducted model test on a scaled array consisting of 3×2 modules connected by ropes, in both regular and irregular wave conditions. Their results indicated that the motion of the six modules remained similar in long waves, with the relative positions between the modules staying unchanged. Wang et al. [25] further validated Jiang’s experimental results through numerical simulations. Their model is a star-type FPV system connected by flexible connectors. The study focused on the impact of different wave conditions and connector parameters on the performance of the FPV system. Luo et al. [26] developed a four-module offshore FPV system concept with soft ropes connection. They conducted model tests and established a numerical model, which was validated against experimental results. The study explored the influence of factors such as module draft, soft rope stiffness, and mooring stiffness on the system’s performance. These primary research on soft connected FPV system serve as important references for advancing research in this field.

In this study, a novel web-type framework for FPV system, as illustrated in Fig. 1, is proposed, and a coupled dynamic response analysis is conducted using the multi-body hydrodynamics and the lumped mass method. Section 2 establishes the model of the proposed concept. Section 3 introduces the time-domain motion equations, wave loads, and connection forces. In Section 4, verification and validation are performed. Section 5 investigates the effects of different wave and design parameters on the modularised arrays in regular waves. Finally, Section 6 summarises the key findings and contributions of this study.

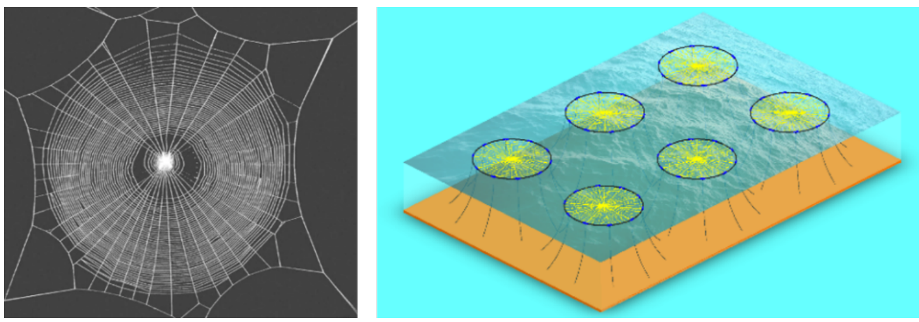

Fig. 1 (a) Geometry of a typical spider web; (b) Web-type floating concept for FPV.

## 2 System description

The basic idea of this paper is inspired by spider webs, with a particular focus on the material properties of its silk and the mechanical characteristics of web-like structures [27]. However, people have not been able to identify an engineering scenario in which this unique and superior web structure can be properly applied. The present work will be the first to systematically study the structural topology of a spider web and explore its application in engineering practice.

The web-type framework introduces a fully flexible design that enables the system to evenly distribute local impact and global wave loads across the entire structure. This holistic load-bearing capability significantly reduces the risk of failure associated with mechanical joints. Besides, the web framework retains its operational integrity even after the failure of one or more ropes, much like the resilience observed in natural spider webs. Furthermore, in comparison to modular systems connected by hinges, the installation and maintenance of add-on devices are expected to be simpler and more cost-effective. The entire system can be easily towed by ships to the installation site, reducing transportation and deployment challenges.

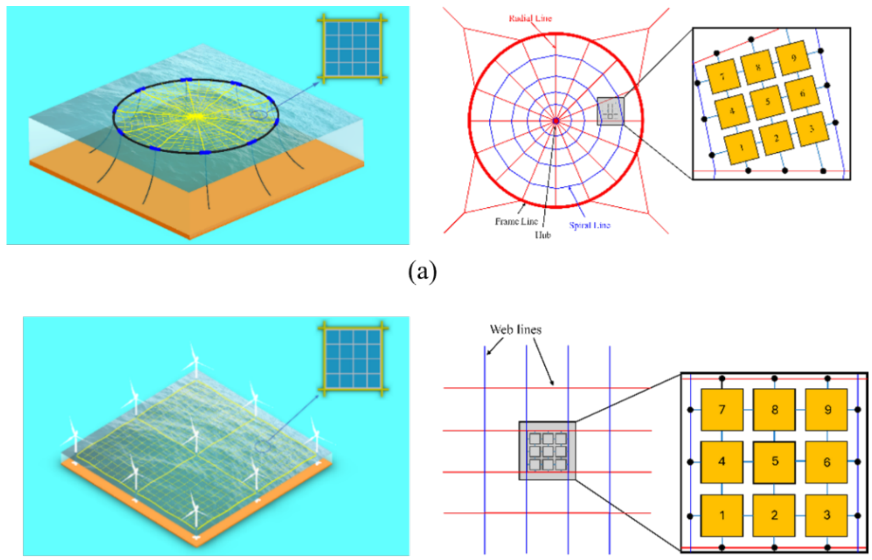


(b)

Fig. 2 Two concepts of web-types of floating solar plant: (a) moored to seabed, and (b) moored to offshore wind turbine foundations.

The flexible web frame, consisting of both spiral and radial lines, allows the system to deform with the waves as a unified structure, as shown in Fig. 2 (a). This deformation enables the system to absorb wave energy through elastic deformation. The elastic ropes made from synthetic materials display time-dependent viscoelastic and viscoelastic behaviour which is dependent on previous load history as well as the applied mean load. Another design, shown in Fig. 2 (b), proposes a possibility to deploy the web structure between offshore wind turbine foundations. These foundations offer an ideal support for the web, enabling effective space utilisation in the offshore area between the turbines. In both designs, the modularised array can be approximately considered to have a square arrangement.

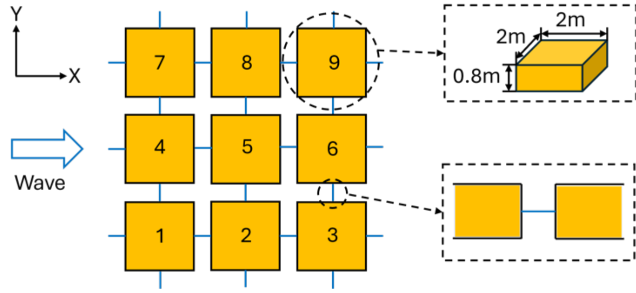


Fig. 3 Configuration of a typical 3×3 FPV array in solar webs.

The wave propagates along the positive *x*-axis direction as shown in Fig. 3. Each module is defined based on body-fixed coordinate system, with origin located at the centre of geometry of a single module. The material of each module substructure supporting the PV system consists of lightweight thermoplastic matrix composites. This material is fully recyclable and has high specific strength and excellent corrosion resistance, which contribute to lower life cycle costs. A lesson learnt from the sea trials of a WEC-PV hybrid system [28] is that the slamming wave loads could easily damage solar panels if there is an airgap between a floater and panel. Therefore, in the present study, the panels are directly mounted onto the top of floaters. In this research, the substructures are modelled as flat boxes with a uniform mass distribution, and the corresponding data is provided in Table 1. Given that their cross-sectional dimensions are significantly smaller than the wavelength, their hydrodynamic loads are estimated using the Morison equation for simplification.

The connection lines used in this study are composed of Polyester rope. As a synthetic material, Polyester does not suffer from corrosion problems and possesses greater tension fatigue, out-of-plane loading and torsion performance than steel components. Due to its low density, Polyester rope requires lighter connecting hardware and reduced structural bracing, resulting in a more efficient system design. The specific parameters of the Polyester rope in this research are provided in Table 2.

Table 1. Physical properties of individual module.

| **Variables** | **Full-scale value** |
|---|---|
| Length (m) | 2.00 |
| Width (m) | 2.00 |
| Height (m) | 0.80 |

| Variables | Full-scale value |
|---|---|
| Material density (kg/m$^3$) | 1025 |
| Draft (m) | 0.40 |
| Gap between modules (m) | 1.0 |
| Total length/width of array (m) | 10 |

Table 2. Physical properties of synthetic rope.

| Variables | Full-scale value |
|---|---|
| Material density (kg/m) | 1.65 (in water) |
| Diameter (mm) | 38 |
| Axial stiffness (kN) | 4.39×10$^3$ |
| Minimum breaking strength (kN) | 219 |
| Safe load (Safe factor=12) (kN) | 18.2 |

The Minimum Breaking Strength (MBS) is the maximum load a rope can withstand before failure, while Safe Load is the maximum load that can be safely applied to the rope during normal operations. It is calculated by applying the safety factor 12 to the MBS.

# 3 Methodology

A RIFLEX model of the web-type platform is created to investigate the load distribution on the ropes. RIFLEX [29] is a computer program for linear and nonlinear analysis of flexible risers and other slender structures. Vertical bar elements are used to model the rigid modules, and horizontal bar elements are used to model the soft rope connection.

## 3.1 Rigid body motions

The modules in a floating array are modelled as rigid bodies. The 6-DoF dynamic equations for a floating rigid body are given as

$$(\boldsymbol{M}+\boldsymbol{\mu}(\infty))\ddot{\boldsymbol{\eta}}(t)+\int_0^t \boldsymbol{h}_{\mathrm{r}}(t-\tau)\dot{\boldsymbol{\eta}}(\tau)d\tau+\boldsymbol{K}\boldsymbol{\eta}(t)=\boldsymbol{f}_{\mathrm{e}}(t)+\boldsymbol{f}_{\mathrm{c}}(t) \quad (1)$$

where $\boldsymbol{M}$ is the body mass matrix; $\boldsymbol{K}$ is the restoring stiffness matrix of a floater. $\boldsymbol{\eta}$, $\dot{\boldsymbol{\eta}}$, and $\ddot{\boldsymbol{\eta}}$ are the displacement, velocity and acceleration vectors respectively. $\boldsymbol{f}_{\mathrm{e}}$ is the wave excitation force. This study only considers the effect of first-order wave loads. $\boldsymbol{f}_{\mathrm{c}}$ is the restoring force from the connection ropes. The hydrodynamic coefficients and external forces are described in their body-fixed coordinates respectively. $\boldsymbol{\mu}(\infty)$ is the added mass matrix at infinite frequency; $\boldsymbol{h}_{\mathrm{r}}$ is the retardation function matrix derived from Cummins' equation, which could be represented as

$$\boldsymbol{h}_{\mathrm{r}}(t) = \frac{2}{\pi}\int_{0}^{\infty} \omega\big(m - \boldsymbol{\mu}_{\mathrm{r}}(\omega)\big)\sin(\omega t)\, d\omega = \frac{2}{\pi}\int_{0}^{\infty} \boldsymbol{\lambda}_{\mathrm{r}}(\omega)\cos(\omega t)\, d\omega \tag{2}$$

where $\boldsymbol{\mu}_{\mathrm{r}}(\omega)$ is the added mass in frequency domain; $\boldsymbol{\lambda}_{\mathrm{r}}(\omega)$ is the added damping in frequency domain.

Assuming the hydrodynamic interactions (radiation and diffraction) are ignored, Morison's equation can be used to estimate the wave loads on each floater. The floating element described in Fig. 3 is modelled as a collection of slender bodies, allowing the wave load on each module to be calculated using the Morison equation. The Morison equation is particularly useful when the structure is small compared to the wavelength of the incoming waves. Typically, the diameter-to-wavelength ratio, $D/L$, should be less than 0.2 to ensure that the structure does not significantly disturb the surrounding flow. The wave load on each module can be calculated by

$$\boldsymbol{f}_{\mathbf{e}}(t) = \frac{1}{2}\rho C_{\mathrm{D}} A u|u| + \rho(1 + C_{\mathrm{A}})V\frac{du}{dt} \tag{3}$$

where $\rho$ is the fluid density, $C_{\mathrm{D}}$ is the drag coefficient, $A$ is the projected area, flow velocity, $C_{\mathrm{A}}$ is the added mass coefficient, is the displaced volume, and $\frac{du}{dt}$ is the acceleration of the flow. The values of $C_{\mathrm{D}}$ and $C_{\mathrm{A}}$ for square cross-sections can be selected according to guidelines provided in DNVGL-RP-C205 [30]. In this model, radiation interactions between bodies are neglected to enhance the computational efficiency.

### 3.2 Lumped mass method

Each floating module is subjected to both hydrodynamic loads and restoring forces generated by the web ropes, which effectively reduce large motion responses under environmental conditions. In this study, a three-dimensional lumped mass method is employed to model the web ropes and mooring line system.

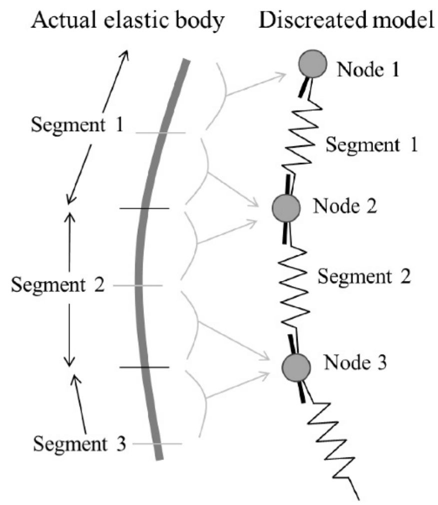


Fig. 4 Model of lumped mass method.

As illustrated in Fig. 4, the lumped mass method calculates tension within lines by dividing the lines into multiple lumped mass points, connected by massless elastic elements. It is assumed that all forces acting on the line are concentrated at these lumped mass points. The line is divided into $n$ segments, with the first end of the first segment connected to the body 1, and the last end of the $n$-th segment connected to body 2. The line is subjected to external forces, including gravity, buoyancy, added mass, and damping forces, all of which are assumed to act on the $n$+1 nodes along the line. The mass of each segment is evenly distributed between the nodes at both ends. The lumped mass points are represented by $p_i$, where the first node is $p_0$, and the last end node is $p_n$. The three-dimensional motion equations of the mooring line are solved using the initial conditions at each point, along with the displacement boundary conditions applied at both ends of the line.

The lines, including both mooring lines and ropes, could be modelled as bar elements in RIFLEX. The spatial bar element is described in a total Lagrangian formulation. The formulation is based on integrated cross-section forces and small strain theory. The element is assumed to be straight with an initial cross-sectional area $A_0$ which is constant along the element length. Each of the two nodes has three translational degrees of freedom, which are expressed directly in the global coordinate system (see Figure 5). The element length is denoted $l_0$ and $l$ in the initial and deformed configuration, respectively. The deformed element length is given by

$$l = \sqrt{\Delta x^2 + \Delta y^2 + \Delta z^2} \tag{4}$$

When the small strain theory is applied, the axial force of the element is given by

$$f_c = \frac{l - l_0}{l_0}(EA) \tag{5}$$

where $l_0$ is initial, stress-free element length, $EA$ is the axial stiffness, $E$ is the material's Young's modulus, $A$ is the cross-sectional area. The strain, $\varepsilon$, is given by

$$\varepsilon = \frac{l - l_0}{l_0} \tag{6}$$

## 3.3 Pretension and clump weight

In scenarios involving floaters connected by soft connections, avoiding collisions is crucial to prevent damage and ensure stability. The clump weight is designed to provide pretension to the rope instead of using tensioning device to elongate the rope. The relationship between weight and pretension obeys the Pythagorean theorem, as shown in Fig. 5.

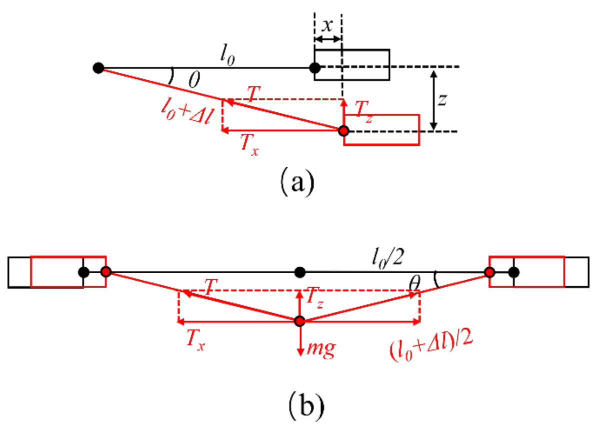


Fig. 5 Relationship of (a) tension and displacement, and (b) pretension and mass of clump weight at equilibrium position. The lumped mass is positioned at the midpoint of the rope.

From the relationship observed in Fig. 5 (a), the tension-displacement relationship in both horizontal ($x$) and vertical ($z$) directions can be expressed as

$$T_x = \frac{EA}{l_0} \frac{\left(\sqrt{(l_0 + x)^2 + z^2} - l_0\right)(l_0 + x)}{\sqrt{(l_0 + x)^2 + z^2}} \tag{7}$$

$$T_z = \frac{EA}{l_0}\frac{\left(\sqrt{(l_0+x)^2+z^2}-l_0\right)z}{\sqrt{(l_0+x)^2+z^2}}$$

From the above functions, it is evident that the relationship between tension and displacement is nonlinear, as is the relationship between pretension and mass. This nonlinearity increases the complexity of the system, making its responses to sinusoidal wave forces inherently nonlinear. As a result, the system does not exhibit simple proportional responses to wave inputs, leading to more complex motion and tension behaviour, particularly under varying open sea environment.

If the heave motion is sufficiently small, the vertical displacement $z$ can be approximated as zero. Under this condition, Eq. (7) can be simplified as

$$T_x = \frac{EA}{l_0}x \qquad T_z = 0 \tag{8}$$

This simplification effectively reduces the system to behave like a linear spring, where the horizontal tension $T_x$ is directly proportional to the horizontal displacement $x$, and no vertical tension is generated due to negligible heave motion.

The clump weight is an equivalence of tension, especially in situation that winch is not easy to install. The relationship between the mass of clump weight and rope tension is described in Fig. 5 (b), and can be expressed as

$$T_x = \frac{l_0}{\sqrt{l^2-(l_0+2x)^2}}mg \qquad T_z = \frac{mg}{2} \tag{9}$$

In operational situations, both sides of the module are subjected to equal pretension from ropes, which keeps the module in its initial position, resulting in $x = 0$. The elongated length $l$ of the rope follows the relationship given in Eq. (7).

## 4 Validations

### 4.1 Validation against diffraction and radiation theory

Despite the wave loads on a cylinder in long waves could be simulated with satisfied fidelity by Morison method in engineering applications, the importance of diffraction and radiation still needs to be quantified. The potential flow theory is well established. With the implementation of a proper numerical scheme, it can be an acknowledged numerical approach with fast solutions and fine precision, being qualified for various hydrodynamic problems without strong nonlinearity.

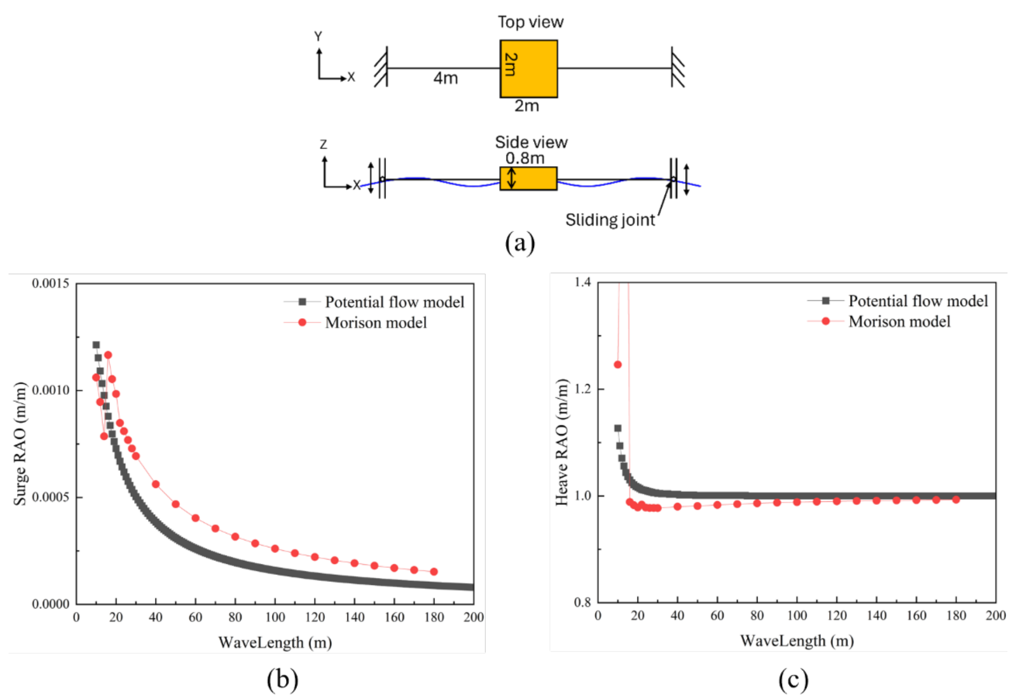


Fig. 6 (a)The single module model for validation, and comparison of (b) Surge RAO and (c) Heave RAO, calculated by potential flow model and Morison model.

For a single box, the surge and heave RAO results are presented in Fig. 6 (a) and (b), and compared with results obtained using potential flow theory with an added linear spring. The spring in potential flow theory is used to model restoring forces, while in the Morison method, a rope serves a similar purpose in a one-dimensional scenario. The linear spring is defined to have the same axial stiffness as the rope. The results show that when using the Morison model, the heave RAO result is close to the potential flow model, and the surge RAO is relatively larger. This difference arises because the rope tension has both horizontal and vertical components as the box floats up and down with the waves, as illustrated in Fig. 5. Consequently, the restoring force from the rope in the $x$ and $z$ directions is a nonlinear function of the surge motion. Additionally, in the Morison model, the selected hydrodynamic parameter, $C_{\mathrm{A}}$, remains constant and does not vary with wave frequency, unlike in potential flow theory where added mass is frequency-dependent. Moreover, the inclusion of the drag coefficient $C_{\mathrm{D}}$ in the Morison model accounts for the viscous effects of water, which potential flow theory neglects.

## 4.2 Validation against tank testing

Following the model test conditions outlined by Jiang et al. [15], the full-scale model test parameters are presented in Table 3, and the simulation model is depicted in Fig. 7.

Table 3. Full-scale model test parameters.

| **Variables** | **Full-scale value** |
|---|---|
| Floater length (m) | 4.70 |
| Floater width (m) | 2.90 |
| Floater height (m) | 0.60 |
| Floater material density (kg/m$^3$) | 313(dry), 352(wet) |
| Free-floating draft (m) | 0.19(dry), 0.21(wet) |
| Array length (m) | 10.4 |
| Array width (m) | 10.7 |
| Gap between floaters (m) | 1.0 |
| Rope material density (kg/m) | 1.8 |

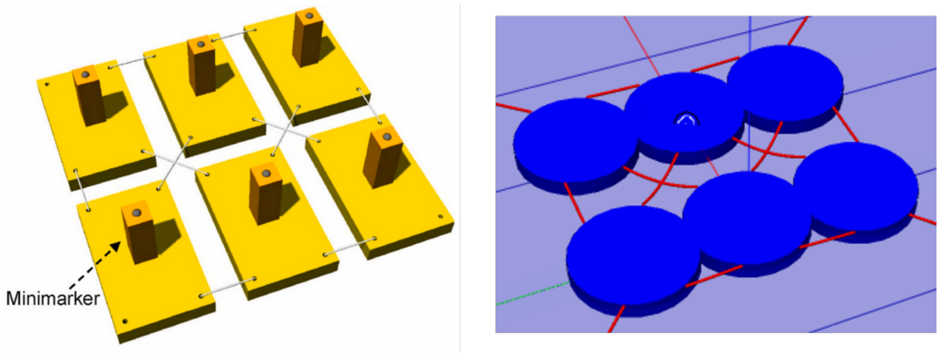


Fig. 7 FPV array model in tank testing and numerical simulation.

The software RIFLEX was used for numerical simulations and compared with the model test results of [15]. The wave conditions are listed in Table 4, and the comparison between the simulation and model test results is illustrated in Figure 7. The boxes are modelled by Morison model as rigid body. For such rectangular cross section whose $L/D$ is 2:1, $C_D$ is set as 1.6 and $C_A$ is set as 1.7 according to DNVGL-RP-C205 [30].

Table 4. Validation conditions.

| **Parameter** | **VC1** | **VC2** | **VC3** | **VC4** | **VC5** |
|---|---|---|---|---|---|
| Wave amplitude (m) | 0.95 | 1.05 | 1.35 | 1.55 | 1.7 |
| Wave period (s) | 7.8 | 8.6 | 9.3 | 10.0 | 10.6 |
| **Parameter** | **VC6** | **VC7** | **VC8** | **VC9** | |
| Wave amplitude (m) | 1.95 | 2.25 | 2.4 | 2.55 | |
| Wave period (s) | 11.2 | 11.8 | 12.3 | 12.8 | |

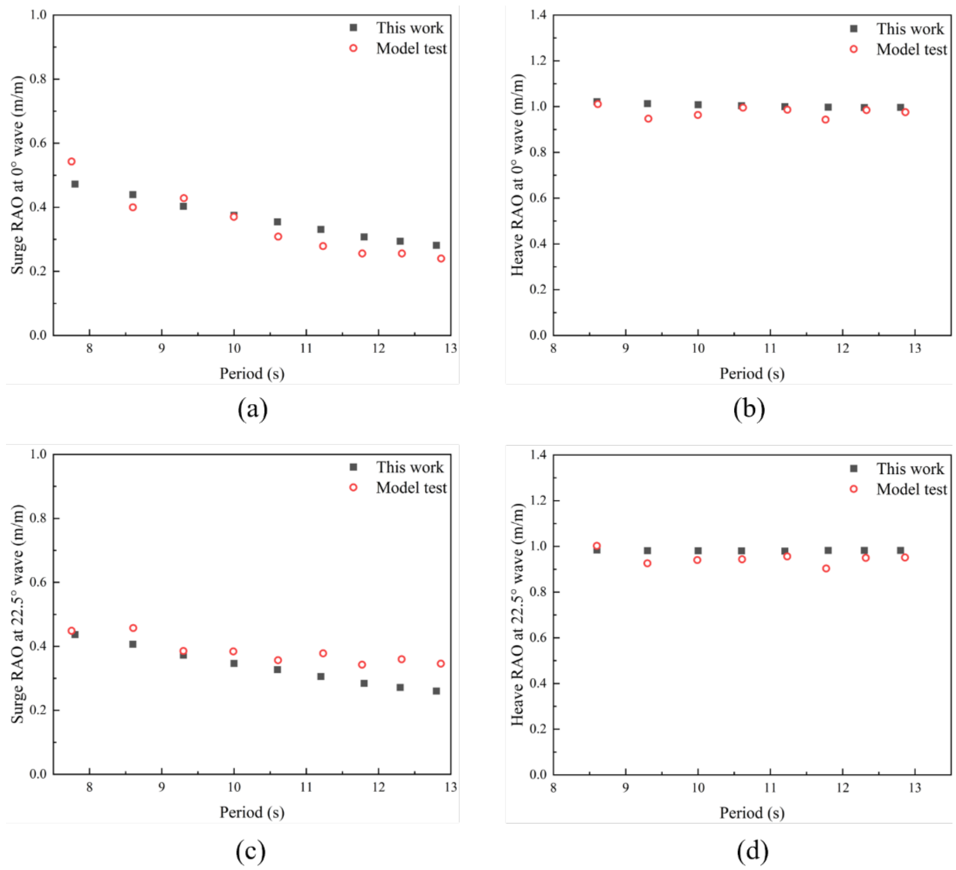


Fig. 8. Validation results between tank test and numerical simulation.

It can be observed in Fig. 8 that for wave incident angles of 0° and 22.5°, the surge and heave motion RAOs are similar to each other. The surge motion RAOs gradually decrease with increasing wave period, while the heave motion RAOs remain around 1 m/m, showing insensitivity to changes in wave period. Although there is slight difference between the numerical simulation and model test results due to various uncertainties in the model test, these differences are within an acceptable range. Thus, the feasibility of the numerical method employed in this study can be confirmed.

## 5 Results and discussion

Due to the array's symmetry, all results exhibit symmetric behaviour, allowing for the calculation of only one-half of the structure when the wave incoming direction is 0°. This discussion will begin with a single line array mainly moving in two-dimensional plane and extend to a three-dimensional array configuration.

## 5.1 Parameter influence on single array

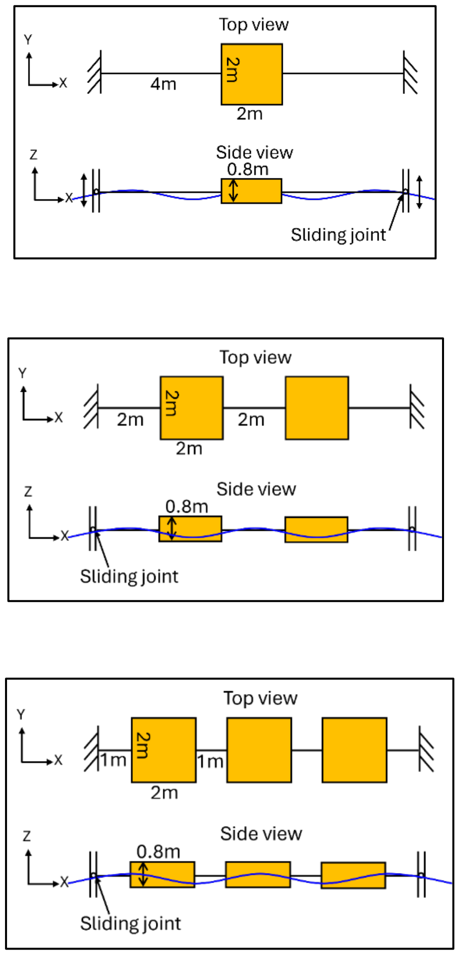


Fig. 9 Configuration of three types of arrays consisting of (a) 1×1 module, (b) 2×1 modules and (c) 3×1 modules.

In this section, three types of arrays containing one, two, and three modules are analysed, as illustrated in **Error! Reference source not found.**. The total length of each array is 10 meters, with the distance between the modules being uniform and equal to the length of the connecting ropes.

### 5.1.1 Wavelength and steepness

The wave conditions are provided in Table 5, with the wave steepness maintained at a constant value of 0.02 across all scenarios.

The ends of the ropes are fixed to tightly tensioned Radial Lines. Under practical wave conditions, vertical motion may occur in Radial Lines, while horizontal displacement is minimal. To more accurately model this, vertical degrees of freedom are released at both ends of the array, allowing for heave motion while maintaining stability in the horizontal plane. This design enables the structure to adapt to wave-induced vertical movements without compromising its overall configuration. No pretension is applied to the system in this section's analysis.

Table 5. Wave conditions.

| **Parameter** | **WC1** | **WC2** | **WC3** | **WC4** | **WC5** | **WC6** | **WC7** | **WC8** |
|---|---|---|---|---|---|---|---|---|
| Wave amplitude (m) | 0.5 | 0.6 | 0.7 | 0.8 | 0.9 | 1.0 | 1.1 | 1.2 |
| Wavelength (m) | 50 | 60 | 70 | 80 | 90 | 100 | 110 | 120 |
| **Parameter** | **WC9** | **WC10** | **WC11** | **WC12** | **WC13** | **WC14** | **WC15** | **WC16** |
| Wave amplitude (m) | 1.3 | 1.4 | 1.5 | 1.6 | 1.7 | 1.8 | 1.9 | 2.0 |
| Wavelength (m) | 130 | 140 | 150 | 160 | 170 | 180 | 190 | 200 |

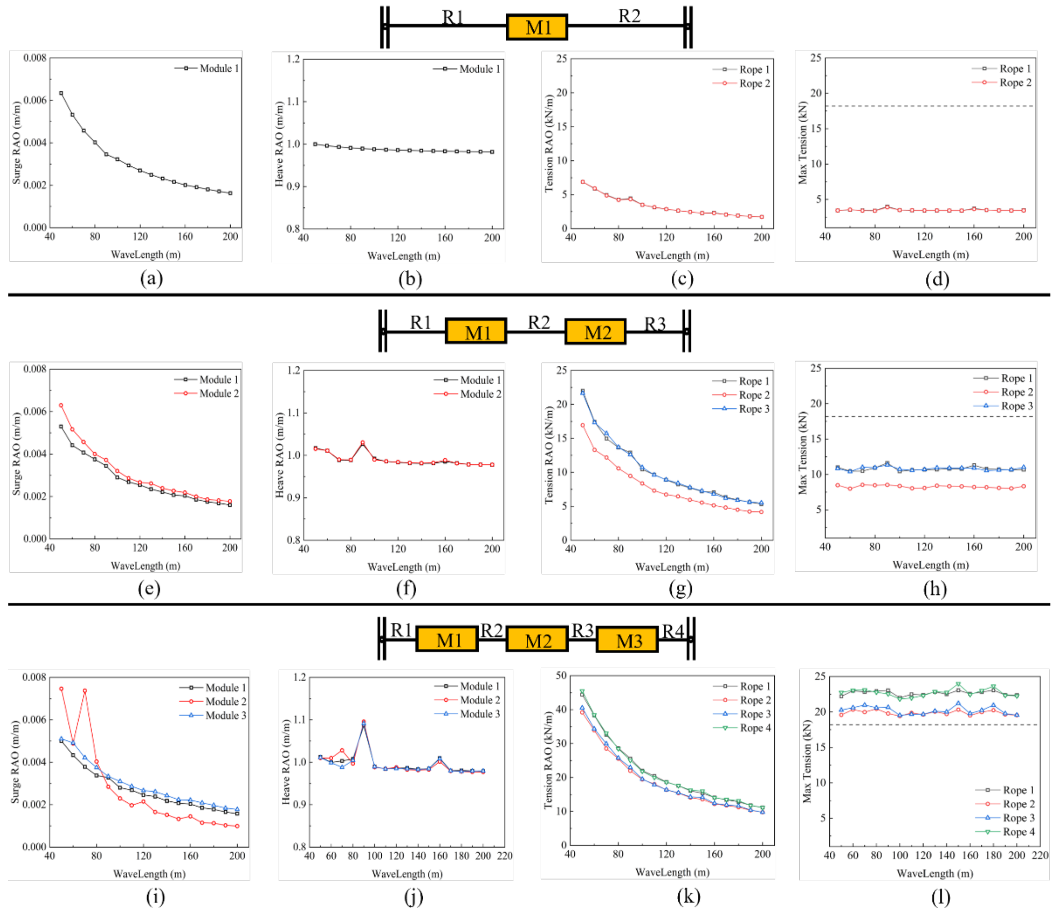


Fig. 10 RAO and tension results with wavelength (wave steepness=0.02).

The surge RAO in Fig. 10 (a), (e), and (i) decreases as the wavelength increases, while the heave RAO varies very slightly near 1 in Fig. 10 (b), (f), and (j). This occurs because the selected wavelength is significantly larger than the characteristic length of the system, causing the heave RAO to gradually stabilise at 1. The overall surge motion is very small due to the restriction provided by the rope, with the surge motion in all cases being less than 1% of the gap between modules. In such case, when a proper pretention is applied to the ropes, there is no risk of collision between floaters.

However, the tension in the ropes presents a significant risk. As shown in Fig. 10 (d), (h), and (l), the maximum tension in the ropes increases dramatically as the rope length decreases across each array configuration. According to Table 2, the safe working load for the selected 38mm rope is 18.2 kN. In the case of the 3×1 array with 1-meter ropes, the maximum tension exceeds this safe load, posing a potential failure risk.

The change in tensions is due to that the rope length directly determines its axial stiffness, as $k = EA/l_0$. As the rope becomes shorter, its stiffness increases, resulting in higher tension under the same loading conditions. Consequently, shorter ropes are subject to greater forces, which can exceed safe working limits, as seen in Fig. 10 (l) for the 3×1 modules.

The results also shows that, the tension in the "interior" ropes is generally lower than in the ropes connected to the boundaries. This is due to the phase difference between the surge motions of the modules. The elongation of the interior ropes is determined by the relative position of the two connected modules, which results in lower tension compared to the boundary ropes.

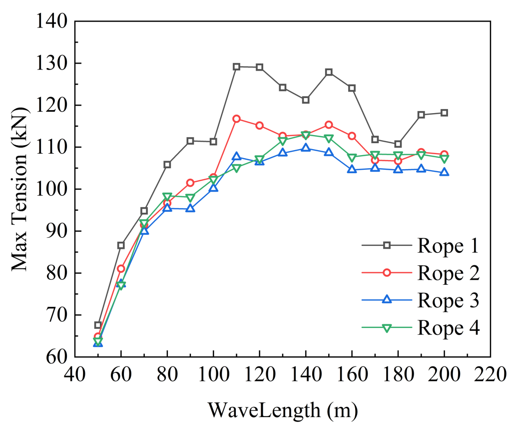


Fig. 11 Rope tensions in the 3×1 array with fixed boundaries.

The motion and tension responses are strongly influenced by whether the boundary points are fixed or free to move vertically. These boundary conditions directly affect the vertical components of rope tensions. Results in Fig. 11 shows that, when the boundaries are fixed, the tension in the system increases significantly. This elevated tension exceeds the safe load limits, introducing excessive stress on the ropes. Allowing more flexible boundary conditions by reducing pretension in frame lines can help mitigate these risks.

The tension response under free boundary conditions has a different variation tendency compared to fixed boundary conditions. In the case of free boundary conditions, the system is less sensitive to changes in wave height, resulting in relatively constant tension values as shown in Fig. 10 (l). Conversely, with fixed boundary conditions, an increase in wave height directly corresponds to higher absolute tension values.

### 5.1.2 Gaps

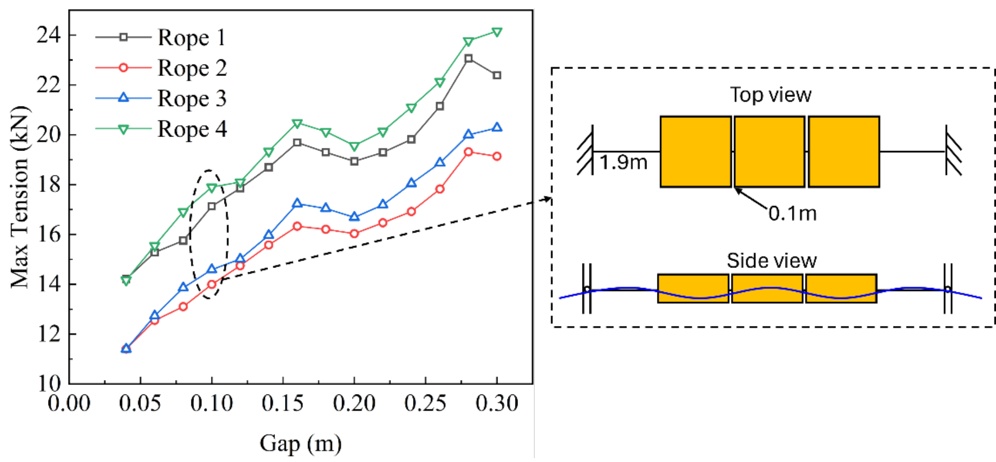


Fig. 12 Relationship between the maximum tension and the gap between modules.

The previous section concludes that the gap, i.e., the rope length, plays a key role in determining the tension in the system. By adjusting the gap, it is possible to redistribute the tension across the ropes. Since the boundary ropes experience higher tension than the interior ropes, increasing the length of the boundary ropes while correspondingly reducing the length of the interior ropes can help balance the load distribution. At an optimal gap, the tensions in all the ropes can be kept below the safe working load.

Take wavelength 100m and the 3-module array for example, the comparison of different gaps is shown in Fig. 12. The relationship between the maximum tension and the gap between modules is not inversely proportional as deducted. For ropes 1 and 4, an increase in length results in a decrease in tension. However, for ropes 2 and 3, the relationship between the maximum tension and gap does not follow this inverse proportionality as initially deduced. A possible reason is that as the modules get closer, the wave phase difference between them decreases. When the modules are positioned closer to one another, their relative motion phases tend to become more synchronized, reducing the relative displacements between them. This synchronization in motion leads to less strain on the connecting ropes, thereby lowering the maximum tension.

### 5.1.3 Pretension

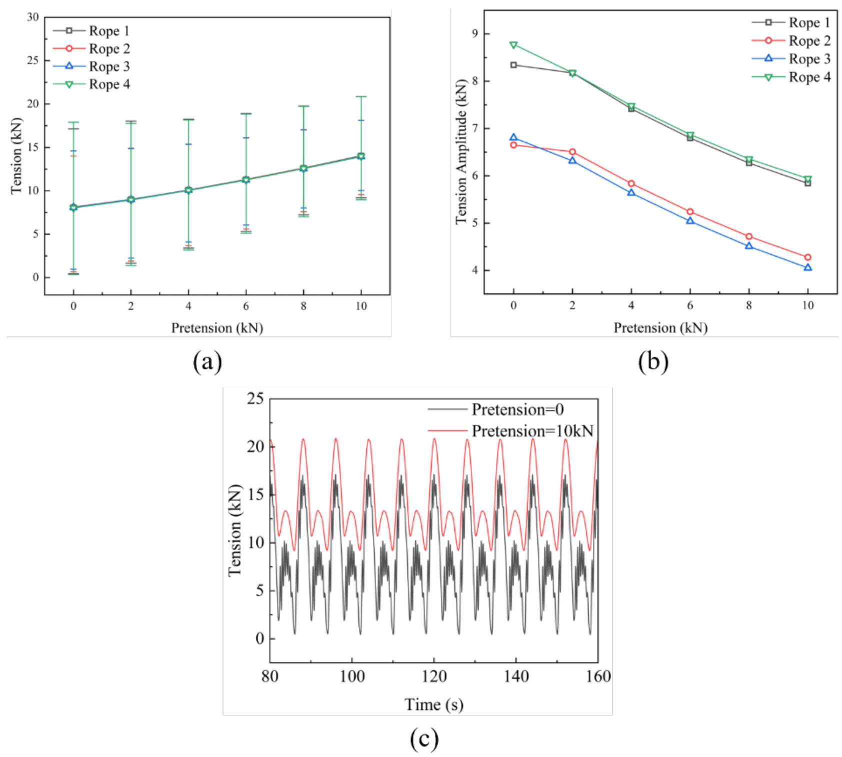


Fig. 13 The variation of (a) Maximum, minimum, and mean tension values, and (b) Tension amplitude, with the change in pretension, and (c) Time domain tension response with and without pretension.

In scenarios where no pretension is applied to the system, rope tensions experience large amplitude variations, which is commonly called “snap load” in rope system. This effect can negatively impact rope durability. To address this, an optimised level of pretension must be applied to ensure the ropes remain taut, thereby preventing the snap effect that occurs when ropes become slack and suddenly tighten.

Various levels of pretension have been explored to determine the optimal configuration, as shown in Fig. 13 (a) and (b). The error bars present the variation between the maximum and minimum tension values. It is evident that the amplitude of tension variation decreases as pretension increases. Although the overall tension level rises, the reduction in tension variation is greater than the increase in absolute tension, demonstrating the effectiveness of pretension in reducing dynamic loads, as shown in (c).

## 5.2 Modularised large array results

### 5.2.1 Wave direction

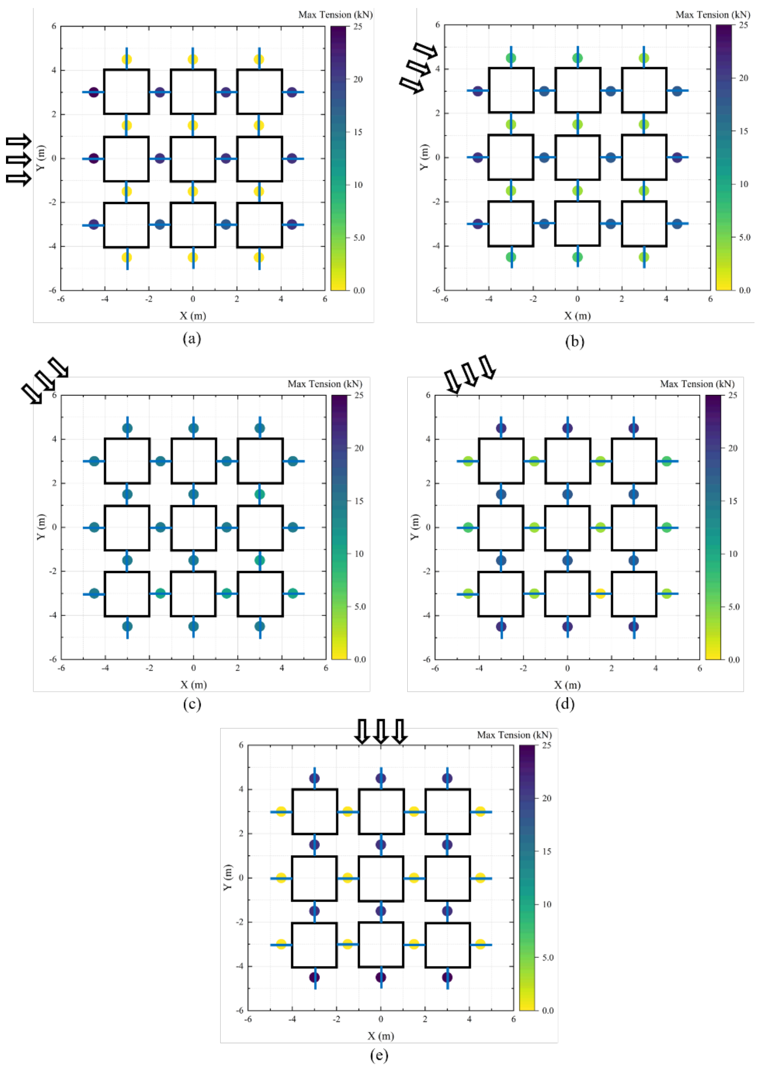


Fig. 14 Distribution of maximum rope tensions in a 3×3 array under 100 m wavelength at wave directions of (a) 0°, (b) 22.5°, (c) 45°, (d) 67.5°, and (e) 90°.

The wave direction is highly related the distribution of rope tensions within the system. The tensions are symmetry along the *x*-axis. When the wave direction is at 0°, the majority of the tension is concentrated in the ropes parallel to the wave propagation direction. As the wave angle increases and more wave components affect the *y*-axis, the tensions in the vertical ropes also increase. At a wave direction of 45°, the tension distribution becomes symmetric along the diagonal of the array. At this wave angle, the tensions are distributed evenly across the array, with all ropes operating within safe load limits. Therefore, the angle must be carefully considered during the installation of the array to avoid overloading the ropes.

### 5.2.2 Rope failure analysis

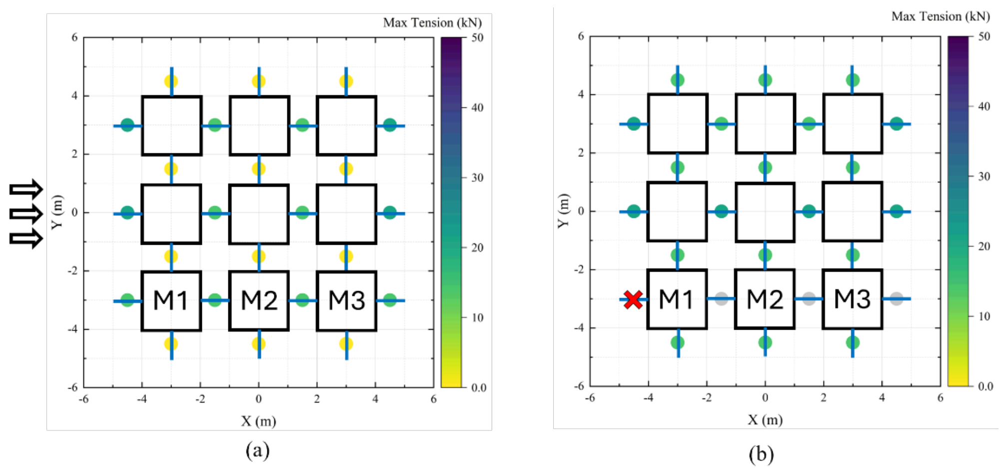


Fig. 15 Distribution of maximum rope tensions in a 3×3 array (a) before failure, (b) after rope 4 failure.

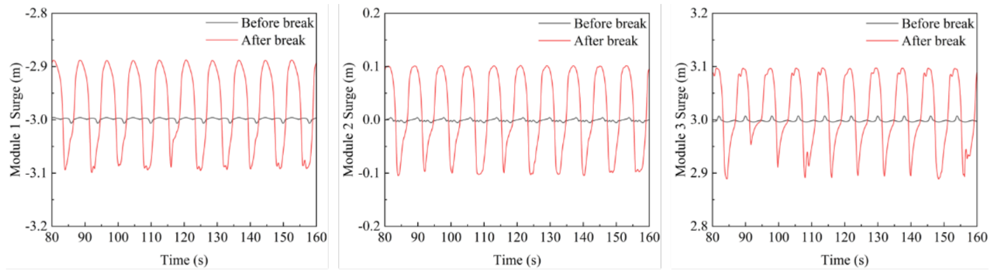


(a) (b) (c)

Fig. 16 The change of surge motion in (a) Module 1, (b) Module 2, and (c) Module 3, before and after break of Rope 4.

The comparison between Fig. 15 (a) and (b) demonstrates that the failure of a horizontal rope results in a dramatic increase in tension within the vertical ropes. Without the horizontal rope's restriction, the surge motion of the modules connected by the broken rope rises significantly, transferring the additional tension to the remaining vertical ropes. This increased surge motion can also lead to snap loads in the ropes aligned horizontally with the failed section. The grey points in Fig. 15 (b) indicate the subsequent failure of other ropes due to the redistributed loads and increased motion.

The surge motions of modules in line with the broken rope are shown in Fig. 16. The absence of tension from Rope 4 cause obvious motion amplification in the Module 1, 2, and 3, which leads to the failure of other horizontal ropes in the same line.

## 6 Conclusions

This paper proposes a new web-type solution for floating photovoltaic systems, focusing on the dynamics of multiple modules interconnected by elastic ropes. The study conducts an analysis of the module array using assumption under Morison model, exploring how configurations influence the system's performance under varying open sea environment.

In the cases of 1×1, 2×1, and 3×1 module configurations, the motion and rope tension responses present similar performance with varying wavelength. When the rope tensions are uniformly distributed, they sufficiently prevent module collisions. However, there exists a risk of failure in the 3×1 array due to the shorter rope lengths. In contrast, under non-uniform distribution with reduced gaps between modules, the tension performance improves. Additionally, the implementation of pretension has been demonstrated to be an effective strategy for mitigating large variations in tension, commonly referred to as “snap loads”.

For the 3×3 module array, the tension distribution is analysed under different wave directions, and when specific ropes experience failure. When the wave propagation direction aligns parallel to any of the ropes, the tension distribution becomes highly unbalanced, significantly increasing the risk of failure. In such scenarios, if any horizontal ropes (aligned with the wave direction) fail, it can lead to the catastrophic failure of the entire line, and a dramatic increase in tension in the vertical ropes (perpendicular to the wave direction).

This limitation of current research is the omission of hydrodynamic interactions between the floating structures for simplicity. In one way, the simplified Morison approach can be improved by implementing a wave transmission model, in which the FPV farm is assumed to be a flexible porous plate [31]. The incoming wave amplitude is subject to a reduction when it propagates along the FOPV farm. In another way, future work could consider using potential flow theory to simulate the dynamics of the floating multi-body system. The radiation interaction needs to be simplified by introducing a truncation scheme [32] to quantify an interactive distance.

## Acknowledgement

This work is part of the International Excellent Young Scientists Programme funded by the National Natural Science Foundation of China (NSFC) with Grant No. W2432030.

## Compliance with ethics guidelines

Zhi-Ming Yuan, Shuang-Rui Yu, and Atilla Incecik declare that they have no conflict of interest or financial conflicts to disclose.

## Reference

[1] Kumar M, Mohammed Niyaz H, Gupta R. Challenges and opportunities towards the development of floating photovoltaic systems. Solar Energy Materials and Solar Cells 2021;233:111408. https://doi.org/10.1016/J.SOLMAT.2021.111408.

[2] Oliveira-Pinto S, Stokkermans J. Assessment of the potential of different floating solar technologies – Overview and analysis of different case studies. Energy Convers Manag 2020;211:112747. https://doi.org/10.1016/J.ENCONMAN.2020.112747.

[3] Essak L, Ghosh A. Floating Photovoltaics: A Review. Clean Technologies 2022;4:752–69. https://doi.org/10.3390/cleantechnol4030046.

[4] Wang J, Lund PD. Review of Recent Offshore Photovoltaics Development. Energies (Basel) 2022;15:7462. https://doi.org/10.3390/en15207462.

[5] Cazzaniga R, Cicu M, Rosa-Clot M, Rosa-Clot P, Tina GM, Ventura C. Floating photovoltaic plants: Performance analysis and design solutions. Renewable and Sustainable Energy Reviews 2018;81:1730–41. https://doi.org/10.1016/J.RSER.2017.05.269.

[6] Wang D, Jin S, Hann M, Conley D, Collins K, Greaves D. Power output estimation of a two-body hinged raft wave energy converter using HF radar measured representative sea states at Wave Hub in the UK. Renew Energy 2023;202:103–15. https://doi.org/10.1016/J.RENENE.2022.11.048.

[7] Huang S, Sheng S, You Y, Gerthoffert A, Wang W, Wang Z. Numerical study of a novel flex mooring system of the floating wave energy converter in ultra-shallow water and experimental validation. Ocean Engineering 2018;151:342–54. https://doi.org/10.1016/J.OCEANENG.2018.01.017.

[8] Yemm R, Pizer D, Retzler C, Henderson R. Pelamis: Experience from concept to connection. Philosophical Transactions of the Royal Society A: Mathematical, Physical and Engineering Sciences 2012;370:365–80. https://doi.org/10.1098/rsta.2011.0312.

[9] Henderson R. Design, simulation, and testing of a novel hydraulic power take-off system for the Pelamis wave energy converter. Renew Energy 2006;31:271–83. https://doi.org/10.1016/j.renene.2005.08.021.

[10] Ma C, Xie S, Bi CW, Zhao YP. Nonlinear dynamic analysis of aquaculture platforms in irregular waves based on Hilbert–Huang transform. J Fluids Struct 2023;117:103831. https://doi.org/10.1016/J.JFLUIDSTRUCTS.2022.103831.

[11] SolarDuck. https://solarduck.tech/ 2022.

[12] CIMC RAFFLES. http://www.cimc-raffles.com/ 2023.

[13] Song J, Kim J, Chung WC, Jung D, Kang YJ, Kim S. Wave-induced structural response analysis of the supporting frames for multiconnected offshore floating photovoltaic units installed in the inner harbor. Ocean Engineering 2023;271:113812. https://doi.org/10.1016/J.OCEANENG.2023.113812.

[14] Yan C, Shi W, Han X, Li X, Verma AS. Assessing the dynamic behavior of multiconnected offshore floating photovoltaic systems under combined wave-wind loads: A comprehensive numerical analysis. Sustainable Horizons 2023;8:100072. https://doi.org/10.1016/J.HORIZ.2023.100072.

[15] Jiang Z, Dai J, Saettone S, Tørå G, He Z, Bashir M, et al. Design and model test of a soft-connected lattice-structured floating solar photovoltaic concept for harsh offshore conditions. Marine Structures 2023;90:103426. https://doi.org/10.1016/J.MARSTRUC.2023.103426.

[16] Dai J, Zhang C, Lim HV, Ang KK, Qian X, Wong JLH, et al. Design and construction of floating modular photovoltaic system for water reservoirs. Energy 2020;191:116549. https://doi.org/10.1016/J.ENERGY.2019.116549.

[17] Noad IF, Porter R. Modelling an articulated raft wave energy converter. Renew Energy 2017;114:1146–59. https://doi.org/10.1016/J.RENENE.2017.07.077.

[18] Zhang D, Du J, Yuan Z, Yu S, Li H. Motion characteristics of large arrays of modularized floating bodies with hinge connections. Physics of Fluids 2023;35. https://doi.org/10.1063/5.0153317.

[19] Shi W, Yan C, Ren Z, Yuan Z, Liu Y, Zheng S, et al. Review on the development of marine floating photovoltaic systems. Ocean Engineering 2023;286:115560. https://doi.org/10.1016/J.OCEANENG.2023.115560.

[20] Wei Y, Zou D, Zhang D, Zhang C, Ou B, Riyadi S, et al. Motion characteristics of a modularized floating solar farm in waves. Physics of Fluids 2024;36. https://doi.org/10.1063/5.0199248.

[21] Ji C, Gao X, Xu S. Study on the influence of connector designs on the hydrodynamic performance of an offshore floating photovoltaic. Ocean Engineering 2024;308:118298. https://doi.org/10.1016/J.OCEANENG.2024.118298.

[22] Ocean Sun. https://oceansun.no/ 2022.

[23] Stainless Steel World. DNV unveils SUNdy floating solar field concept. http://st ainless-steel-world.net 2022.

[24] Trapani K, Millar DL. The thin film flexible floating PV (T3F-PV) array: The concept and development of the prototype. Renew Energy 2014;71:43–50. https://doi.org/10.1016/J.RENENE.2014.05.007.

[25] Wang B, Li Y, Huang L, Yao Y, Qin Y. Dynamic analysis of a novel star-type floating photovoltaic system with flexible connectors. Ocean Engineering 2024;304:117854. https://doi.org/10.1016/J.OCEANENG.2024.117854.

[26] Luo W, Zhang X, Tian X, Cheng Z, Wen B, Li X, et al. Conceptual design and model test of a pontoon-truss type offshore floating photovoltaic system with soft connection. Ocean Engineering 2024;309:118518. https://doi.org/10.1016/J.OCEANENG.2024.118518.

[27] Cranford SW, Tarakanova A, Pugno NM, Buehler MJ. Nonlinear material behaviour of spider silk yields robust webs. Nature 2012;482:72–6. https://doi.org/10.1038/nature10739.

[28] Versey MJ, Kiprakis A, Retzler C. Experimental results from the hybridisation of wave and solar energy to provide consistent power to islanded loads. 11th International Conference on Renewable Power Generation - Meeting net zero carbon (RPG 2022), Institution of Engineering and Technology; 2022, p. 53–7. https://doi.org/10.1049/icp.2022.1656.

[29] MARINTEK. Riflex Theory Manual, Version 4.24.2. 2023.

[30] DNVGL-RP-C205. Environmental conditions and environmental loads. 2017.

[31] Koley S. Water wave scattering by floating flexible porous plate over variable bathymetry regions. Ocean Engineering 2020;214:107686. https://doi.org/10.1016/J.OCEANENG.2020.107686.

[32] Zhang D, Yuan ZM, Du J, Li H. Hydrodynamic modelling of large arrays of modularized floating structures with independent oscillations. Applied Ocean Research 2022;129. https://doi.org/10.1016/j.apor.2022.103371.